




# Mechanism of ammonia synthesis on $\text{Fe}_3\text{Mo}_3\text{N}^\dagger$

Michael D. Higham, \*<sup>ab</sup> Constantinos D. Zeinalipour-Yazdi, <sup>d</sup>  
Justin S. J. Hargreaves<sup>e</sup> and C. Richard A. Catlow <sup>abc</sup>

Received 7th November 2022, Accepted 21st November 2022

DOI: 10.1039/d2fd00148a

Ammonia ( $\text{NH}_3$ ) synthesis is an essential yet energy-demanding industrial process. Hence, there is a need to develop  $\text{NH}_3$  synthesis catalysts that are highly active under milder conditions. Metal nitrides are promising candidates, with the  $\eta$ -carbide  $\text{Co}_3\text{Mo}_3\text{N}$  having been found to be more active than the industrial Fe-based catalyst. The isostructural  $\text{Fe}_3\text{Mo}_3\text{N}$  catalyst has also been identified as highly active for  $\text{NH}_3$  synthesis. In the present work, we investigate the catalytic ammonia synthesis mechanisms in  $\text{Fe}_3\text{Mo}_3\text{N}$ , which we compare and contrast with the previously studied  $\text{Co}_3\text{Mo}_3\text{N}$ . We apply plane-wave density functional theory (DFT) to investigate surface N vacancy formation in  $\text{Fe}_3\text{Mo}_3\text{N}$ , and two distinct ammonia synthesis mechanisms. The calculations reveal that whilst N vacancy formation on  $\text{Fe}_3\text{Mo}_3\text{N}$  is more thermodynamically demanding than for  $\text{Co}_3\text{Mo}_3\text{N}$ , the formation energies are comparable, suggesting that surface lattice N vacancies in  $\text{Fe}_3\text{Mo}_3\text{N}$  could facilitate  $\text{NH}_3$  synthesis.  $\text{N}_2$  activation was found to be enhanced on  $\text{Fe}_3\text{Mo}_3\text{N}$  compared to  $\text{Co}_3\text{Mo}_3\text{N}$ , for adsorption both at and adjacent to the vacancy. The calculated activation barriers suggest that, as for  $\text{Co}_3\text{Mo}_3\text{N}$ , the associative Mars van Krevelen mechanism affords a much less energy-demanding pathway for ammonia synthesis, especially for initial hydrogenation processes.

## Introduction

Ammonia ( $\text{NH}_3$ ) synthesis is one of the most important industrial chemical processes, most notably for the production of fertilisers, which are crucial to supporting agriculture, and therefore ensuring global food security. With the world population estimated at 7.6 billion people in 2021, and projected to reach over 11 billion people by the end of the century, it is all but certain that ammonia

<sup>a</sup>University College London, Department of Chemistry, Kathleen Lonsdale Building, Gower Place, London, WC1E 6BT, UK. E-mail: m.higham@ucl.ac.uk

<sup>b</sup>Research Complex at Harwell, Rutherford Appleton Laboratory, Harwell, Oxon, OX11 0FA, UK

<sup>c</sup>School of Chemistry, Cardiff University, Park Place, Cardiff, CF10 1AT, UK

<sup>d</sup>University of East London, University Way, London, E16 2RD, UK

<sup>e</sup>University of Glasgow, School of Chemistry, Glasgow, G12 8QQ, UK

<sup>†</sup> Electronic supplementary information (ESI) available. See DOI: <https://doi.org/10.1039/d2fd00148a>



synthesis will remain a high priority for the chemical industry.<sup>1,2</sup> Indeed, industry reports conclude that 80% of all ammonia produced is consumed by the agricultural sector, with an estimated 178 330 kilotons being produced in 2021 alone,<sup>3</sup> and it is estimated that over the past century, 27% (ref. 4) of the world's population has been supported by food produced using ammonia-based fertilisers.<sup>4,5</sup> Consequently, ammonia synthesis is also one of the most environmentally challenging industrial processes, with ammonia production being responsible for an estimated 1.8% of global energy consumption, and the same proportion of global CO<sub>2</sub> emissions;<sup>6</sup> producing one tonne of NH<sub>3</sub> consumes an estimated 30 GJ of energy, and releases 2.3 tonnes of CO<sub>2</sub>.<sup>7,8</sup> Furthermore, between 3–5% of global consumption of natural gas can be attributed to ammonia production, making reducing the environmental impact of ammonia synthesis even more urgent in light of instability of global gas supplies.<sup>9</sup>

Since the early 20th century, the Haber–Bosch process<sup>10</sup> has been employed to produce ammonia on an industrial scale, relying on promoted iron-based catalysts and high temperature and pressure conditions (400–500 °C, 100–200 atm), which account for the high energy consumption of this process. As such, the quest to develop highly active and stable catalysts for ammonia synthesis that can operate under milder conditions is a key scientific challenge, with even relatively minor enhancements in performance translating into significant reductions in environmental and economic cost. It has been demonstrated that the ammonia synthesis reaction on Fe-based catalysts proceeds *via* a dissociative Langmuir–Hinshelwood (LH) mechanism, which involves the first process, the dissociation of adsorbed N<sub>2</sub>, being the most activated, and therefore rate determining, process,<sup>11,12</sup> with a similar mechanism being identified for the more active, but more costly, Ru-based system.<sup>13,14</sup> The high activation barrier associated with the rate determining N<sub>2</sub> dissociation process can be attributed to the high bond dissociation energy (946 kJ mol<sup>-1</sup>), and accounts for the high temperature and pressure conditions required by the Haber–Bosch process. Hence, novel catalysts that provide an alternative, more energetically accessible, reaction mechanism, afford a viable avenue for developing highly active ammonia synthesis catalysts that can operate under milder conditions.<sup>15</sup>

Transition metal nitrides have emerged as promising candidate catalysts for ammonia synthesis,<sup>16</sup> spanning a wide range of materials of different structure and composition.<sup>17–25</sup> The ternary metal nitride, Co<sub>3</sub>Mo<sub>3</sub>N, is an especially promising candidate material,<sup>26–31</sup> exhibiting even greater activity than the industrial Fe-based catalyst when suitably promoted.<sup>27</sup> It has been suggested that the remarkable activity of this system can be wholly attributed to the inherent activities of metallic Co and Mo towards N<sub>2</sub> binding; both of these elements are expressed in the Co<sub>3</sub>Mo<sub>3</sub>N(111) surface, and linear scaling relations from previous studies show that the average of the N<sub>2</sub> binding energies for metallic Co and Mo is close to the supposed optimum for ammonia synthesis.<sup>29</sup> However, further experimental studies show that lattice N in Co<sub>3</sub>Mo<sub>3</sub>N is highly active,<sup>32</sup> and could therefore facilitate ammonia synthesis by enabling a Eley–Rideal–Mars–van-Krevelen (ER–MvK) type mechanism, whereby lattice nitrogen is continually consumed (and evolved as the product, ammonia) and replenished (from the reactant gas phase nitrogen). A series of detailed computational studies explored the possibility of nitrogen vacancy formation on Co<sub>3</sub>Mo<sub>3</sub>N surfaces, and investigated both the traditional LH mechanism, and the novel ER–MvK mechanism, for



ammonia synthesis; the calculations revealed that surface N vacancy formation is indeed highly plausible, and that the novel ER–MvK mechanism affords a highly kinetically accessible mechanism for ammonia synthesis, with significantly lower activation barriers for key elementary processes.<sup>15,33–36</sup>

The Fe<sub>3</sub>Mo<sub>3</sub>N system, which is isostructural to Co<sub>3</sub>Mo<sub>3</sub>N, has also been found to be highly active for ammonia synthesis.<sup>37,38</sup> However, experimental studies show that, in contrast to the isostructural Co system, Fe<sub>3</sub>Mo<sub>3</sub>N appears to be highly resistant to reduction, with no appreciable loss of lattice N being observed even under harsh conditions.<sup>39</sup> Furthermore, experimental studies also show that the quaternary metal nitride system (Co<sub>3–x</sub>Fe<sub>x</sub>Mo<sub>3</sub>N) is highly active towards ammonia synthesis,<sup>38</sup> opening the possibility to finely tune ammonia synthesis activity by determining the optimal Co:Fe ratio. Clearly, a detailed understanding of both the Co and Fe ternary systems is required before embarking on the rational design of an optimal quaternary metal nitride catalyst.

It is therefore of considerable interest to explore the mechanisms for ammonia synthesis on Fe<sub>3</sub>Mo<sub>3</sub>N, analogous to the previous studies for Co<sub>3</sub>Mo<sub>3</sub>N, both to rationalise the high activity of the Fe<sub>3</sub>Mo<sub>3</sub>N ternary metal nitride, and to inform future investigations into the quaternary Co<sub>3–x</sub>Fe<sub>x</sub>Mo<sub>3</sub>N system. In the present work, plane-wave density functional theory techniques are applied to explore surface N vacancy formation, and both the dissociative LH mechanism, and associative ER–MvK mechanism, for Fe<sub>3</sub>Mo<sub>3</sub>N. The calculations reveal that surface N vacancy formation is feasible for the Fe<sub>3</sub>Mo<sub>3</sub>N system, and that N<sub>2</sub> activation takes place both at and adjacent to surface N vacancy sites. The calculations also show that, as for Co<sub>3</sub>Mo<sub>3</sub>N, the associative ER–MvK mechanism provides a more energetically accessible mechanistic pathway for ammonia synthesis. The present work, in addition to providing key insights into the behaviour of the Fe<sub>3</sub>Mo<sub>3</sub>N system, will serve as a benchmark study for future work exploring promotion of the Fe<sub>3</sub>Mo<sub>3</sub>N catalyst, and (in tandem with the previous work for the Co<sub>3</sub>Mo<sub>3</sub>N system) for investigations concerning the quaternary Co<sub>3–x</sub>Fe<sub>x</sub>Mo<sub>3</sub>N system, supporting the rational design of optimal metal nitride catalysts for ammonia synthesis.

## Methodology

All calculations were performed using plane-wave density functional theory (DFT) as implemented in the VASP code (version 5.4.4).<sup>40–43</sup> A thin-film Fe<sub>3</sub>Mo<sub>3</sub>N (111) model was constructed exposing a nitrogen-rich termination, based on the model successfully developed for the isostructural Co<sub>3</sub>Mo<sub>3</sub>N system reported in previous computational studies.<sup>15,33,35</sup> The optimised lattice parameter for bulk Fe<sub>3</sub>Mo<sub>3</sub>N was determined in previous studies<sup>33</sup> and was used to define the dimensions of the surface slab periodic cell. The thin-film slab consists of a 2 × 2 surface supercell, to minimise lateral interactions between adsorbed species in adjacent periodic images, and three N-containing layers forming a non-stoichiometric symmetric slab model, as illustrated in Fig. 1. The thin film slab was centred in the periodic cell, with a vacuum separation of 30 Å between slabs in adjacent periodic images, ensuring sufficient slab separation to avoid any spurious interactions. During geometry optimisation, all atomic positions were allowed to relax. In line with the previous computational studies for Co<sub>3</sub>Mo<sub>3</sub>N, a *Γ*-centred (4 × 4 × 1) Monkhorst–Pack *k*-point sampling scheme was used.<sup>15,44</sup> Inner electrons were



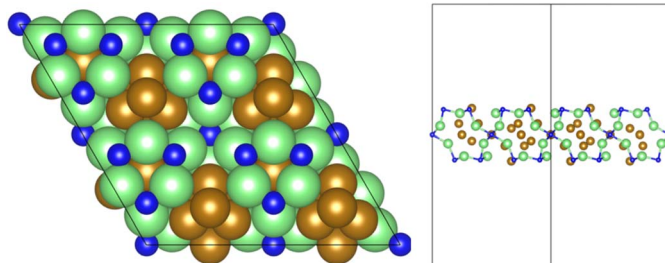


Fig. 1 Graphic illustrating the symmetric, non-stoichiometric thin-film slab model used to model the  $\text{Fe}_3\text{Mo}_3\text{N}$  surface, from the top (left) and side (right), as viewed across the cell diagonal. The pristine surface is illustrated, *i.e.* no N vacancies are present. Key: green, Mo; brown, Fe; blue, N.

replaced by projector-augmented waves (PAW),<sup>45,46</sup> and the valence states were expanded in plane-waves with a cut-off energy of 650 eV. The revised PBE (RPBE) exchange correlation functional was used throughout, having previously been demonstrated to accurately reproduce  $\text{N}_2$  bond dissociation energy,<sup>15</sup> with a dispersion correction applied using the D3 scheme devised by Grimme, and Becke–Johnson damping, in order to account for the weak van der Waals interactions responsible for the physisorption behaviour of species such as  $\text{N}_2$ .<sup>47,48</sup>

In order to investigate the elementary reaction processes involved in the LH and ER–MvK mechanisms for ammonia synthesis, optimised geometries were obtained for all adsorbed reactants, products, and intermediates, on the  $\text{Fe}_3\text{Mo}_3\text{N}$  (111) surface model featuring a single surface N vacancy, with atomic forces converged to within  $0.01 \text{ eV } \text{\AA}^{-1}$ . In each case, electronic wavefunctions were converged such that the total energy was converged to within  $10^{-5} \text{ eV}$ . Transition states were identified using the climbing image nudged elastic bands (CI-NEB) and dimer methods, with vibrational analysis confirming that a saddle point had indeed been located.

For the *ab initio* thermodynamics study, calculated DFT electronic energies were combined with gas-phase thermochemistry data (obtained from the NIST Webbook<sup>49</sup>) using the general approach described by Reuter *et al.*<sup>50</sup> to obtain the Gibbs free energy of vacancy formation as a function of  $\text{H}_2$  partial pressure and temperature, to estimate typical surface N vacancy concentrations under a range of hydrogenating conditions. Further details of the *ab initio* thermodynamics model can be found in the ESI.†

## Results

### Formation of surface N vacancies

As illustrated in the previous studies investigating the  $\text{Co}_3\text{Mo}_3\text{N}$  system, the possibility of an associative MvK-type mechanism depends on the presence of surface N vacancies to activate adsorbed  $\text{N}_2$ . As such, it is of interest to calculate the N vacancy formation energy, both with respect to  $\text{N}_2$  and  $\text{NH}_3$  arising from hydrogenation of surface lattice N under appropriate conditions, to determine the overall thermodynamic feasibility of the vacancy formation. The calculated nitrogen vacancy formation energies are presented in Table 1, for both a single N



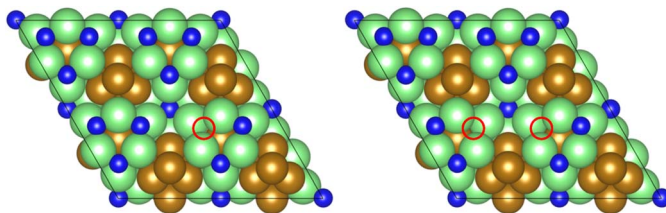


Fig. 2 Graphic illustrating the model surface with a single N vacancy present (left) and two adjacent N vacancies (right). The locations of the N vacancies are highlighted by the red circles.

**Table 1** Calculated N vacancy formation energies, for a single vacancy and two adjacent vacancies, with respect to both evolution of  $N_2$ , and evolution of  $NH_3$  by reacting with  $H_2$ . The vacancy formation energy per N vacancy is also presented

N vacancy	$\Delta E_{vac. ref.}$	$\Delta E_{vac. ref.}$	$\Delta E_{vac. ref.}$	$\Delta E_{vac. ref.}$
	$N_2/eV$	$NH_3/eV$	$N_2$ per N/eV	$NH_3$ per N/eV
1	1.893	0.972	1.893	0.972
2	4.247	2.406	2.124	1.203

vacancy, and two adjacent N vacancies to determine the extent of lateral instability; Fig. 2 illustrates both the surface with a single N vacancy and two adjacent N vacancies.

The calculated vacancy formation energies show that, with respect to the formation of  $N_2$ , the formation of a single N vacancy on the model surface is endothermic by 1.893 eV. For the formation of two adjacent vacancies, a value of 4.247 eV was obtained, giving a formation energy per N vacancy of 2.124 eV, indicating that there is only a moderate extent of repulsive interaction between adjacent N vacancies, with the vacancy formation energy per vacancy differing by only 0.231 eV; hence, it may be possible to achieve appreciable surface N vacancy concentrations under appropriate conditions.

For the vacancy formation energies with respect to  $H_2$  and  $NH_3$ , we find that the vacancy formation energy is considerably less endothermic, with a vacancy formation energy of only 0.972 eV for a single N vacancy, and 1.203 eV per vacancy for two adjacent N vacancies, suggesting that, under ammonia synthesis conditions where  $H_2$  is present, formation of N vacancies *via* evolution of  $NH_3$  should be more thermodynamically feasible compared to the formation of N vacancies *via* evolution of  $N_2$  under comparable conditions where  $H_2$  is not present.

### **Ab initio thermodynamics of vacancy formation under hydrogenation conditions**

Whilst the calculated vacancy formation energies for both  $Co_3Mo_3N$  and  $Fe_3Mo_3N$  are endothermic, the DFT calculated energies do not account for temperature and pressure dependent thermodynamic contributions under real conditions; in the case of lattice N being evolved into the gas phase to form surface vacancies, it is clear that entropy contributions arising both from translational and rotational



degrees of freedom of gas phase molecules, and configurational entropy arising from many possible permutations of larger numbers of surface vacancies, will have a considerable impact on the thermodynamic feasibility of vacancy formation. To this end, we apply *ab initio* thermodynamics techniques to extrapolate the DFT results to provide approximate insights into the extent of surface N vacancy formation under a range of possible experimental conditions, based on the established approach detailed in previous works investigating a variety of different systems;<sup>51–54</sup> details of the *ab initio* thermodynamics model are described in detail in the ESI.†

The thin-film  $\text{Fe}_3\text{Mo}_3\text{N}$  (111) model used in the present work consists of two surfaces of  $248.46 \text{ \AA}^2$ , which corresponds to  $2.49 \times 10^{-22} \text{ cm}^2$ , giving a total surface area of  $4.97 \times 10^{-22} \text{ cm}^2$ . The  $(2 \times 2)$  surface supercell presents a total of 24 surface lattice N atoms, 12 for each side of the slab. Hence, the range of vacancy concentrations represented by the model spans from  $2.01 \times 10^{21} \text{ cm}^{-2}$  (for a single vacancy) to  $4.83 \times 10^{22} \text{ cm}^{-2}$  (for the maximum surface vacancy concentration, *i.e.* all 24 surface N atoms in the thin film model having been removed). Fig. 3 shows the approximate vacancy concentration for varying  $\text{H}_2$  partial pressure and temperatures,<sup>55</sup> based on the calculated Gibbs free energy of vacancy formation for each vacancy concentration representable within the thin-film model.

The *ab initio* thermodynamic studies summarised in Fig. 3 show that N vacancy concentration is higher at higher  $\text{H}_2$  partial pressures and higher temperatures, as expected. Whilst the model is necessarily limited to a minimum vacancy concentration of  $2.01 \times 10^{21} \text{ cm}^{-2}$  (this being the vacancy concentration corresponding to a single surface N vacancy within the  $2 \times 2$  thin film model), it

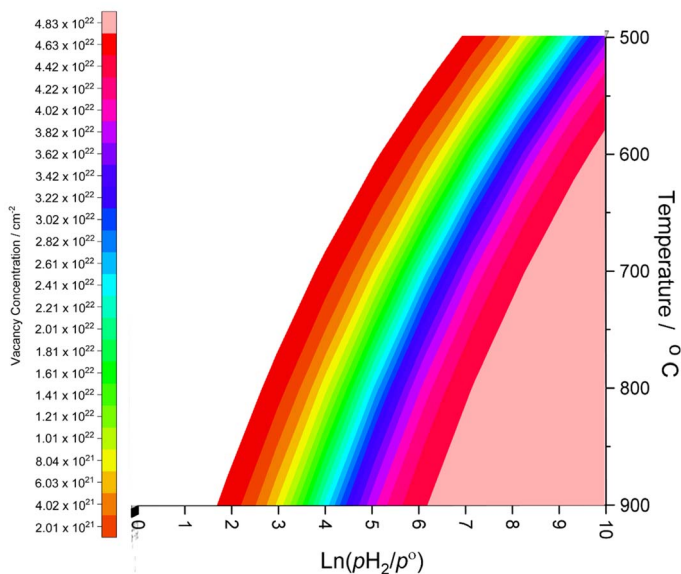


Fig. 3 Surface N vacancy concentration as a function of  $\text{H}_2$  partial pressure (where  $p^\circ$  is ambient pressure) and temperature, as estimated from *ab initio* thermodynamics.



can still be seen that one would not necessarily expect an appreciable number of vacancies to be formed under ambient pressure ( $\ln\left(\frac{p^{\text{H}_2}}{p^\circ}\right) \cong 0$ ) for any range of temperatures. However, even at relatively modest  $\text{H}_2$  partial pressures, such as 10 mPa,<sup>56,57</sup> which is at the lower range of pressures applied for ammonia synthesis using the industrially well-established Fe-based catalysts ( $\ln\left(\frac{p^{\text{H}_2}}{p^\circ}\right) \cong 4.5$ ), the *ab initio* thermodynamics suggest that the  $2.01 \times 10^{21} \text{ cm}^{-2}$  vacancy concentration threshold would be reached at 650 °C. It is therefore highly plausible that lower concentrations of surface N vacancies would be present at somewhat lower temperatures and pressures and could therefore facilitate ammonia synthesis *via* the ER–MvK mechanism.

### Associative Eley–Rideal–Mars–van-Krevelen mechanism

As illustrated from the DFT calculations for vacancy formation, and resulting *ab initio* thermodynamics studies, it is likely that there is an appreciable vacancy concentration on the  $\text{Fe}_3\text{Mo}_3\text{N}$  (111) surface under relatively mild experimental conditions. Hence, it is of interest to explore the energetics of the ER–MvK mechanism for this system that was found to afford a more kinetically accessible pathway for ammonia synthesis for the isostructural  $\text{Co}_3\text{Mo}_3\text{N}$  system.<sup>35</sup>

The calculated reaction energies and activation barriers with corresponding frequencies for the unstable mode are presented in Table 2.

The mechanism proceeds with the initial associative adsorption of the  $\text{N}_2$  molecule at the vacancy site (process 1), as illustrated in Fig. 4. This adsorption process is highly exothermic, at  $-1.746 \text{ eV}$ , and induces a considerable elongation of the  $\text{N}_2$  bond, to  $1.320 \text{ \AA}$ , compared to the  $1.098 \text{ \AA}$  determined experimentally,<sup>58</sup> indicating a substantial degree of activation of the  $\text{N}_2$  molecule.

The initial hydrogenation process takes place *via* an Eley–Rideal mechanism with direct hydrogenation of the adsorbed  $\text{N}_2$  species by  $\text{H}_2$  from the gas phase

**Table 2** DFT calculated reaction energies, activation barriers, and vibrational frequencies for unstable modes corresponding to the reaction coordinate, for all elementary processes associated with the Eley–Rideal–Mars–van-Krevelen mechanism for ammonia synthesis. The N vacancy adsorption site is indicated by the symbol  $\square$  in the chemical equations for each elementary process, with intermediates adsorbed at the vacancy site indicated using this symbol in superscript. Co-adsorbed species located at adsorption sites other than the N vacancy site are indicated by \*

Process number	Process	$\Delta E/\text{eV}$	$E_A/\text{eV}$	$\nu/\text{cm}^{-1}$
1	$\square + \text{N}_2(\text{g}) \rightarrow \text{N}_2^\square$	-1.746	—	—
2	$\text{N}_2^\square + \text{H}_2(\text{g}) \rightarrow \text{N}_2\text{H}_2^\square$	-0.753	—	—
3	$\text{N}_2\text{H}_2^\square + \text{H}_2(\text{g}) \rightarrow \text{N}_2\text{H}_2^\square + \text{H}_2^*$	-0.286	—	—
4	$\text{N}_2\text{H}_2^\square + \text{H}_2^* \rightarrow \text{N}_2\text{H}_3^\square + \text{H}^*$	0.290	1.269	1361.892
5	$\text{N}_2\text{H}_3^\square + \text{H}^* \rightarrow \text{N}^\square + \text{H}^* + \text{NH}_3(\text{g})$	-0.274	—	—
6	$\text{N}^\square + \text{H}^* \rightarrow \text{NH}^\square$	-0.812	0.373	1310.662
7	$\text{NH}^\square + \text{H}_2(\text{g}) \rightarrow \text{NH}^\square + \text{H}_2^*$	-0.315	—	—
8	$\text{NH}^\square + \text{H}_2^* \rightarrow \text{NH}_2^\square + \text{H}^*$	1.013	1.590	1195.889
9	$\text{NH}_2^\square + \text{H}^* \rightarrow \text{NH}_3^\square$	-0.229	0.430	1191.220
10	$\text{NH}_3^\square \rightarrow \square + \text{NH}_3(\text{g})$	1.272	—	—



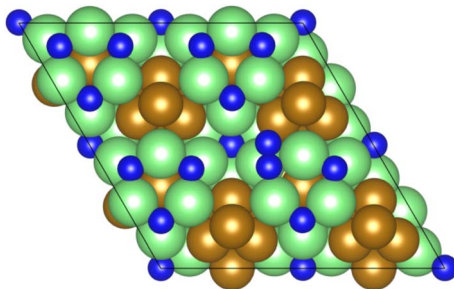


Fig. 4 Graphic illustrating the associative adsorption of  $N_2$  at the surface N vacancy site.

(Table 2, process 2), yielding the  $N_2H_2^\square$  intermediate (Fig. 5). The process is exothermic by  $-0.753$  eV and lacks an intrinsic barrier due to the high energy of the incident  $H_2$  molecule.

Subsequently, a second equivalent of  $H_2$  is exothermically adsorbed ( $-0.286$  eV) adjacent to the  $N_2H_2^\square$  (Table 2, process 3), undergoing dissociation synchronously with the formation of a new N-H bond to yield the  $N_2H_3^\square$  intermediate (Table 2, process 4), with this process having a much higher activation barrier (1.269 eV), reflecting the saturation of the N-N bond with successive hydrogenation, although the process is only mildly endothermic (0.290 eV), as illustrated in Fig. 6.

Dissociation of the N-N bond of the  $N_2H_3^\square$  intermediate evolves the first equivalent of ammonia, the process is exothermic (Table 2, process 5,  $-0.274$  eV)

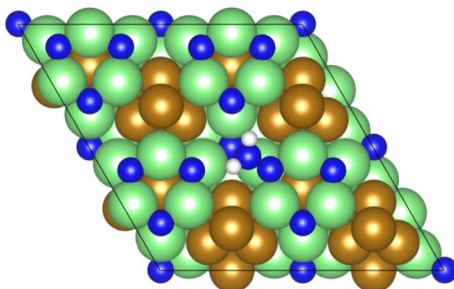


Fig. 5 Graphic illustrating the adsorption configuration of the  $N_2H_2^\square$  intermediate.

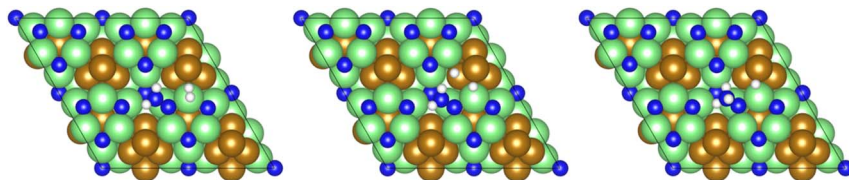


Fig. 6 Graphics illustrating the initial (left), transition (centre), and final (right) state geometries associated with hydrogenation of the  $N_2H_2^\square$  intermediate to yield the  $N_2H_3^\square$  intermediate (Table 2, process 4).





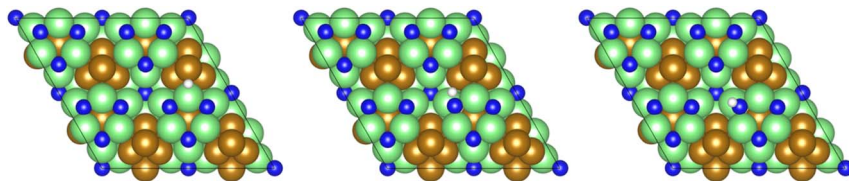


Fig. 7 Graphics illustrating the initial (left), transition (centre), and final (right) state geometries associated with hydrogenation of surface lattice N (regenerated after the evolution of a first equivalent of  $\text{NH}_3$ ) to yield the  $\text{NH}^\square$  intermediate (Table 2, process 6).

and leaves the remaining N atom originating from the adsorbed  $\text{N}_2$  molecule in process 1 located in the vacancy site, essentially replacing the lattice N lost during vacancy formation, and a co-adsorbed H atom. These co-adsorbed species subsequently form the  $\text{NH}^\square$  intermediate (Table 2, process 6, Fig. 7), the process being moderately exothermic ( $-0.812$  eV), and again, only weakly activated ( $0.373$  eV).

The third and final equivalent of  $\text{H}_2$  required to complete the catalytic cycle is then adsorbed exothermically ( $-0.315$  eV) in a similar manner to process 3 (Table 2, process 7), before again dissociating and forming a second N–H bond to yield the  $\text{NH}_2^\square$  (Table 2, process 8); the process is moderately endothermic ( $1.013$  eV) and has a considerable activation barrier of  $1.590$  eV, making this the most energy-demanding elementary process in the ER–MvK mechanism by a considerable margin, and thus we would expect this process to also be the rate determining elementary step in this catalytic cycle (Fig. 8). It must also be noted that whilst the activation barrier for this hydrogenation process is high, and therefore represents a significant kinetic obstacle to formation of the second equivalent of ammonia to regenerate the surface vacancy, at this stage in the reaction mechanism a first equivalent of ammonia has already been evolved. Hence, it is entirely possible that ammonia synthesis could proceed identically to that described by processes 1 to 5 in Table 2 at a different N vacancy site. Such behaviour would correspond to N looping, rather than true catalysis, since in this scenario the N vacancies are not regenerated within the same cycle, but could be under a different set of conditions.

The remaining hydrogenation process then takes place, yielding the  $\text{NH}_3^\square$  intermediate (Table 2, process 9), which is conversely mildly exothermic ( $-0.229$  eV) and has only a moderate activation barrier ( $0.430$  eV), illustrated in Fig. 9.

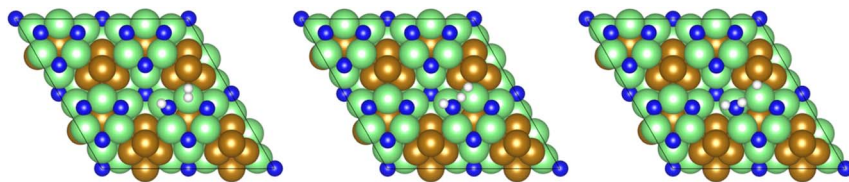


Fig. 8 Graphics illustrating the initial (left), transition (centre), and final (right) state geometries associated with hydrogenation of the  $\text{NH}_2^\square$  intermediate to yield the  $\text{NH}_3^\square$  intermediate (Table 2, process 8).



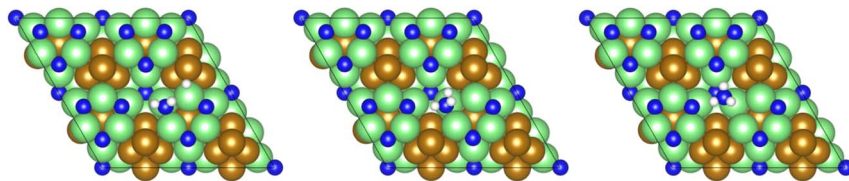


Fig. 9 Graphics illustrating the initial (left), transition (centre), and final (right) state geometries associated with hydrogenation of the  $\text{NH}_2^\square$  intermediate to yield the  $\text{NH}_3^\square$  (Table 2, process 9).

Evolution of the second equivalent of ammonia completes the catalytic cycle, regenerating the surface lattice N vacancy, this process being considerably endothermic by 1.272 eV.

The calculated reaction profile for the ER-MvK mechanism reveals that the presence of a surface lattice N vacancy is indeed able to significantly activate  $\text{N}_2$ , and the initial hydrogenation processes are facile, with generally low activation barrier. Conversely, higher activation barriers and more energy-demanding processes are observed for the final hydrogenation processes and evolution of the second equivalent of ammonia. Hence, whilst the surface lattice N vacancies are clearly highly active, their formation (with the latter processes of the mechanism essentially corresponding to the hydrogenation of lattice N to yield the surface vacancy) presents a greater challenge for overall feasibility of the reaction mechanism.

### Dissociative Langmuir–Hinshelwood mechanism

Having explored the associative ER-MvK mechanism, it is also of interest to consider the possibility of the dissociative LH mechanism providing an alternative pathway for ammonia synthesis, to afford comparison both with the ER-MvK

Table 3 DFT calculated reaction energies, activation barriers, and vibrational frequencies for unstable modes corresponding to the reaction coordinate, for all elementary processes associated with the dissociative Langmuir–Hinshelwood mechanism for ammonia synthesis

Process number	Process	$\Delta E/\text{eV}$	$E_A/\text{eV}$	$\nu/\text{cm}^{-1}$
1	$\text{N}_2(\text{g}) \rightarrow \text{N}_2^*$	-0.172	—	—
2	$\text{N}_2^* \rightarrow 2\text{N}^*$	-0.436	0.708	453.952
3	$2\text{N}^* + \text{H}_2(\text{g}) \rightarrow 2\text{N}^* + 2\text{H}^*$	-1.372	—	—
4	$2\text{N}^* + 2\text{H}^* \rightarrow \text{NH}^* + \text{N}^* + \text{H}^*$	0.027	1.480	1263.294
5	$\text{NH}^* + \text{N}^* + \text{H}^* \rightarrow \text{NH}_2^* + \text{N}^*$	0.104	1.143	1095.821
6	$\text{NH}_2^* + \text{N}^* + \text{H}_2(\text{g}) \rightarrow \text{NH}_2^* + \text{N}^* + 2\text{H}^*$	-0.885	—	—
7	$\text{NH}_2^* + \text{N}^* + 2\text{H}^* \rightarrow \text{NH}_3^* + \text{N}^* + \text{H}^*$	0.282	1.329	886.360
8	$\text{NH}_3^* + \text{N}^* + \text{H}^* \rightarrow \text{N}^* + \text{H}^* + \text{NH}_3(\text{g})$	1.405	—	—
9	$\text{N}^* + \text{H}^* \rightarrow \text{NH}^*$	-0.600	0.532	1192.142
10	$\text{NH}^* + \text{H}_2(\text{g}) \rightarrow \text{NH}^* + 2\text{H}^*$	-1.349	—	—
11	$\text{NH}^* + 2\text{H}^* \rightarrow \text{NH}_2^* + \text{H}^*$	-0.012	1.206	999.554
12	$\text{NH}_2^* + \text{H}^* \rightarrow \text{NH}_3^*$	0.910	1.636	1169.424
13	$\text{NH}_3^* \rightarrow \text{NH}_3(\text{g})$	0.258	—	—



on  $\text{Fe}_3\text{Mo}_3\text{N}$ , and the LH mechanism on the  $\text{Co}_3\text{Mo}_3\text{N}$  system which has been extensively investigated previously.<sup>35</sup>

The calculated reaction energies and activation barriers with corresponding frequencies for the unstable mode are presented in Table 3. The initial process, as for the associative ER–MvK mechanism, consists of adsorption of the  $\text{N}_2$  molecule, although in the associative LH mechanism,  $\text{N}_2$  is adsorbed adjacent to, rather than at, the surface N vacancy site.

The adsorption of  $\text{N}_2$  adjacent to the vacancy site is weakly exothermic ( $-0.172$  eV, Table 3, process 1), considerably less so than for adsorption at the vacancy, although notably there is still evidence of  $\text{N}_2$  activation even when the  $\text{N}_2$  molecule is merely adsorbed near, rather than at, the surface N vacancy site, with an elongation of the  $\text{N}_2$  bond length being observed,  $1.359$  Å compared to  $1.098$  Å determined experimentally,<sup>58</sup> even greater than that observed for  $\text{N}_2$  adsorbed at the N vacancy site as investigated in the ER–MvK mechanism. This result suggests that the presence of surface N vacancies is able to facilitate  $\text{N}_2$  activation even when adsorption takes place outside the immediate vicinity of surface N vacancies.

The dissociation of the adsorbed  $\text{N}_2$  molecule (Table 3, process 2), which has been identified as the rate-limiting elementary process for ammonia synthesis on Fe<sup>11,12</sup> and Ru<sup>13,14</sup> based catalysts, is only moderately activated on the  $\text{Fe}_3\text{Mo}_3\text{N}$  (111) surface, with a calculated activation barrier of  $0.708$  eV, and the process is exothermic by  $-0.436$  eV, reflecting the considerable  $\text{N}_2$  activation even when  $\text{N}_2$  is not adsorbed directly at the surface N vacancy site (Fig. 10). The resulting  $\text{N}^*$  species are adsorbed at two distinct surface sites: the first being a 3-coordinate Mo–Fe–Mo site, subsequently referred to as the Fe–Mo interface; whilst the second is located at a 3-coordinate Mo-only site, adjacent to the lattice N vacancy. We will first consider hydrogenation of  $\text{N}^*$  at the Fe–Mo interfacial site.

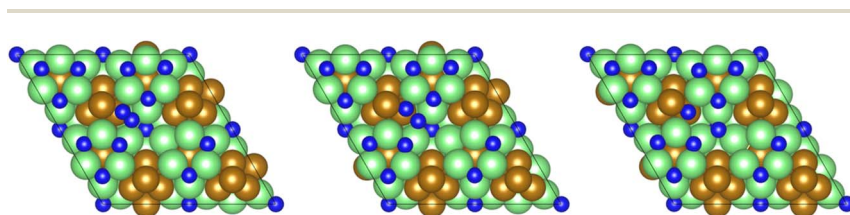


Fig. 10 Graphics illustrating the initial (left), transition (centre), and final (right) state geometries associated with  $\text{N}_2$  dissociation (Table 3, process 2).

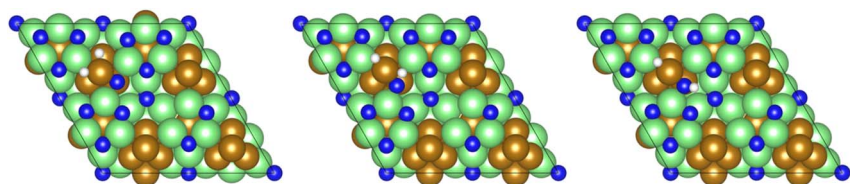


Fig. 11 Graphics illustrating the initial (left), transition (centre), and final (right) state geometries associated with the first  $\text{N}^*$  hydrogenation process (Table 3, process 4).



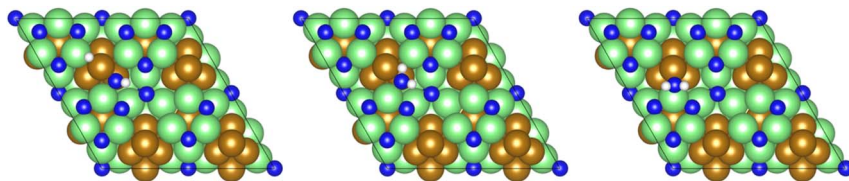


Fig. 12 Graphics illustrating the initial (left), transition (centre), and final (right) state geometries associated with the first  $\text{NH}^*$  hydrogenation process (Table 3, process 5).

Exothermic dissociative adsorption of  $\text{H}_2$  ( $-1.372$  eV, Table 3, process 3) is followed by hydrogenation of one of the  $\text{N}^*$  resulting from  $\text{N}_2$  dissociation (Table 3, process 4). Whilst the process is almost thermoneutral ( $0.027$  eV), it also has a high activation barrier ( $1.480$  eV), presenting a significant energetic barrier to initial N hydrogenation, as illustrated in Fig. 11.

This pattern continues for the second hydrogenation process to yield  $\text{NH}_2^*$  (Fig. 12), which is also mildly endothermic ( $0.104$  eV) and has a high activation barrier of  $1.143$  eV (Table 3, process 5), albeit somewhat lower than for the preceding hydrogenation process. It was also seen that during the hydrogenation process,  $\text{NH}^*$  shifts from the 3-coordinate Fe–Mo interfacial site with  $\text{NH}_2^*$  being formed at a 2-coordinate Fe–Mo site.

A second equivalent of  $\text{H}_2$  is then dissociatively adsorbed on the surface exothermically ( $-0.885$  eV, Table 3, process 6), and subsequently hydrogenation of the  $\text{NH}_2^*$  intermediate takes place to yield  $\text{NH}_3^*$  (Table 3, process 7). As for the preceding hydrogenation processes,  $\text{NH}_3^*$  formation is only slightly endothermic ( $0.282$  eV) but has a high activation barrier of  $1.329$  eV. During hydrogenation,  $\text{NH}_2^*$  shifts once again such that the resulting  $\text{NH}_3^*$  species adopts a 1-coordinate adsorption environment located slightly offset from the top of the Fe atom, as illustrated in Fig. 13.

Evolution of the first equivalent of ammonia is strongly endothermic ( $1.405$  eV, Table 3, process 8), and is followed by the first hydrogenation of the second  $\text{N}^*$  (Table 3, process 9); in contrast to the corresponding process for the first  $\text{N}^*$  (Table 3, process 4), this process is exothermic by  $-0.600$  eV, and has only a moderate activation barrier of  $0.532$  eV. It is notable that the first series of hydrogenation processes (Table 3, processes 4, 5, 7), which were all determined to be endothermic and highly activated, took place at the  $\text{N}^*$  species located at the Fe–Mo interface, whilst hydrogenation of the second  $\text{N}^*$  species (Table 3, process 9; Fig. 14), involves  $\text{N}^*$  migrating from a 3-coordinate Mo site to the Fe–Mo

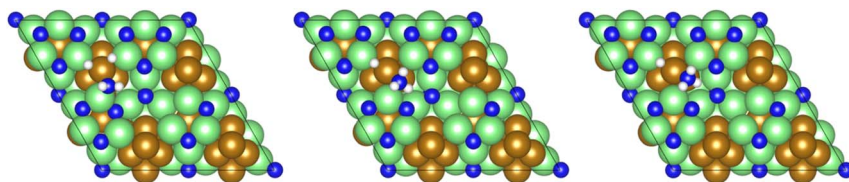


Fig. 13 Graphics illustrating the initial (left), transition (centre), and final (right) state geometries associated with the first  $\text{NH}_2^*$  hydrogenation process (Table 3, process 7).



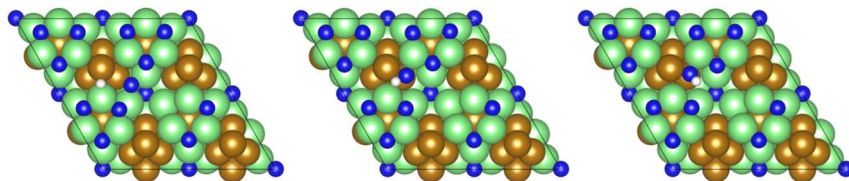


Fig. 14 Graphics illustrating the initial (left), transition (centre), and final (right) state geometries associated with the second  $N^*$  hydrogenation process (Table 3, process 9).

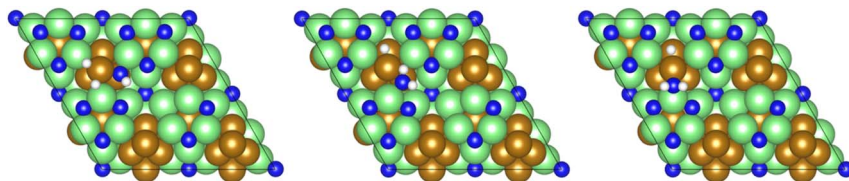


Fig. 15 Graphics illustrating the initial (left), transition (centre), and final (right) state geometries associated with the second  $NH^*$  hydrogenation process (Table 3, process 11).

interface. This implies that the  $N^*$ ,  $NH^*$ , and  $NH_2^*$  species are more stabilised at the Fe–Mo interface site, and therefore these species are more resistant to hydrogenation at this site, compared to at the 3-coordinate Mo site.

Dissociative adsorption of the third and final equivalent of  $H_2$  takes place exothermically ( $-1.349$  eV, Table 3, process 10). Subsequently,  $NH^*$  undergoes hydrogenation to  $NH_2^*$  (Table 3, process 11), this process being found to be almost thermoneutral ( $-0.012$  eV), and a return to the high activation barriers calculated for the first series of hydrogenation processes is observed, with an activation barrier of  $1.206$  eV being determined; once again, during hydrogenation the  $NH^*$  species moves from the 3-coordinate Fe–Mo interfacial site to form  $NH_2^*$  at the adjacent 2-coordinate Fe–Mo bridging site (Fig. 15), in a manner virtually identical to that determined for process 4.

The final hydrogenation process (Table 3, process 12; Fig. 16) to form  $NH_3^*$  occurs analogously to process 7, being even more endothermic ( $0.910$  eV) and having a high activation barrier of  $1.636$  eV, making this the most energy-demanding elementary process in the dissociative LH mechanism.

Finally, evolution of the second equivalent of ammonia (Table 3, process 13) completes the catalytic cycle, and is mildly endothermic at  $0.258$  eV.

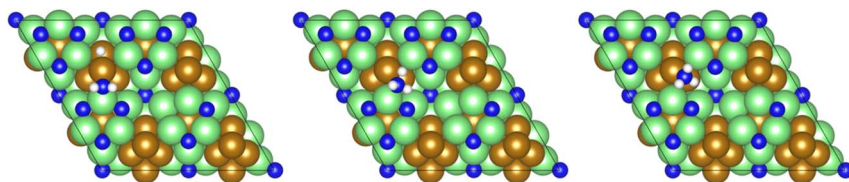


Fig. 16 Graphics illustrating the initial (left), transition (centre), and final (right) state geometries associated with the second  $NH_2^*$  hydrogenation process (Table 3, process 12).



The calculations for the dissociative LH mechanism for ammonia synthesis reveal that whilst the initial adsorption and dissociation of  $N_2$  is enhanced on the  $Fe_3Mo_3N$  (111) surface, subsequent hydrogenation processes are largely highly activated and endothermic, especially at the Mo–Fe interfacial surface site; indeed the only hydrogenation process that deviates from this is process 9, which involves hydrogenation of the  $N^*$  species from the Mo-only site, with the remaining endothermic hydrogenation processes largely being compensated by highly exothermic dissociative adsorption of  $H_2$ .

## Discussion

The computed reaction profiles for the two mechanisms are presented in Fig. 17. It is clear that whilst  $N_2$  adsorption and activation (and dissociation, for the LH type mechanism) is enhanced both at and adjacent to the surface N vacancy, the subsequent hydrogenation processes are far less activated for the associative ER–MvK mechanism, at least for the initial hydrogenation processes; indeed, the only elementary process in the ER–MvK mechanism with an activation barrier greater than 1 eV is the second  $NH^*$  hydrogenation process (Table 2, process 8), whilst for the LH mechanism, the only hydrogenation process with an activation barrier less 1 eV is the second  $N^*$  hydrogenation process (Table 3, process 9). Hence, it appears likely that the high activity of  $Fe_3Mo_3N$  can be attributed to this mechanism, and therefore N vacancy formation in  $Fe_3Mo_3N$  is confined to the surface (as suggested by the bulk N/vacancy diffusion calculations), explaining the negligible loss of lattice N in  $Fe_3Mo_3N$  reported experimentally, in stark contrast with  $Co_3Mo_3N$ . Here, we will compare the two mechanisms and the two ternary metal nitride systems, comparing and contrasting the results, and offering some insight to rationalise the experimentally reported phenomena in light of the calculations presented in the present work and previous literature.

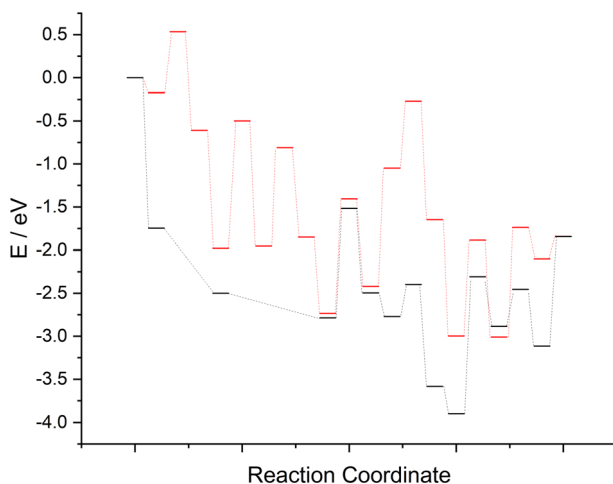


Fig. 17 Computed reaction profile for the two mechanisms for ammonia synthesis on  $Fe_3Mo_3N$ , for the associative Eley–Rideal–Mars–van–Krevelen mechanism (black) and the dissociative Langmuir–Hinshelwood mechanism (red).



## Surface formation and bulk diffusion of N vacancies

In comparison with the vacancy formation energies for  $\text{Co}_3\text{Mo}_3\text{N}$  in the literature,<sup>15</sup> the corresponding  $\text{Co}_3\text{Mo}_3\text{N}(111)$  surface N vacancy formation energy was calculated to be 1.68 eV, only 0.21 eV less endothermic than for  $\text{Fe}_3\text{Mo}_3\text{N}$ . Whilst this is in agreement with the experimental findings that lattice N in  $\text{Fe}_3\text{Mo}_3\text{N}$  is generally less active compared to  $\text{Co}_3\text{Mo}_3\text{N}$ ,<sup>38,39,59</sup> it is notable that the modest difference in the calculated vacancy formation energies for the two compounds suggests that formation of surface N vacancies on  $\text{Fe}_3\text{Mo}_3\text{N}$  is at the very least highly plausible, which is consistent with the experimental observation that bulk lattice N in  $\text{Fe}_3\text{Mo}_3\text{N}$  is inactive, if loss of lattice N is confined only to the surface layers, and therefore accounts for only a negligible loss of total lattice nitrogen from the experimental sample. Hence, this finding suggests that the experimentally observed resistance of  $\text{Fe}_3\text{Mo}_3\text{N}$  to loss of lattice N under high temperature hydrogenation conditions can be attributed to the diffusion of bulk and subsurface lattice nitrogen to the surface being kinetically, rather than thermodynamically, unfeasible.

## $\text{N}_2$ activation

Comparison of the  $\text{N}_2$  adsorption process between the  $\text{Fe}_3\text{Mo}_3\text{N}$  and  $\text{Co}_3\text{Mo}_3\text{N}$  shows that  $\text{N}_2$  activation is considerably enhanced on  $\text{Fe}_3\text{Mo}_3\text{N}$ , with  $\text{N}_2$  adsorption both at the surface N vacancy site, and adjacent to the N vacancy site, being more exothermic than for  $\text{Co}_3\text{Mo}_3\text{N}$ . Adsorption of  $\text{N}_2$  at the surface N vacancy is exothermic by  $-1.746$  eV (Table 2, process 1), compared to a mere  $\sim -0.73$  eV for  $\text{Co}_3\text{Mo}_3\text{N}$ , whilst at the site adjacent to the vacancy, the process is exothermic by  $-0.172$  eV for  $\text{Fe}_3\text{Mo}_3\text{N}$  (Table 3, process 1), and slightly endothermic for  $\text{Co}_3\text{Mo}_3\text{N}$  ( $+0.42$  eV).<sup>35</sup> The enhanced  $\text{N}_2$  activation for  $\text{Fe}_3\text{Mo}_3\text{N}$  can be interpreted in terms of its more endothermic vacancy formation energy (Table 1) compared to  $\text{Co}_3\text{Mo}_3\text{N}$ , implying that the defective system is inherently less stable, and therefore more active, for the Fe system compared to the Co system. Despite the considerably more exothermic adsorption energies on the  $\text{Fe}_3\text{Mo}_3\text{N}$  surface, the elongation of the  $\text{N}_2$  bond is comparable between the Fe and Co systems, both when  $\text{N}_2$  is adsorbed at the N vacancy site ( $1.320$  Å for  $\text{Fe}_3\text{Mo}_3\text{N}$ , compared to  $1.297$  Å for  $\text{Co}_3\text{Mo}_3\text{N}$ ) and when  $\text{N}_2$  is adsorbed adjacent to the vacancy site ( $1.359$  Å for  $\text{Fe}_3\text{Mo}_3\text{N}$ , compared to  $1.363$  Å for  $\text{Co}_3\text{Mo}_3\text{N}$ ). For both the Fe and Co systems, activation of  $\text{N}_2$  adjacent to the N vacancy also can be seen to play a key role in facilitating  $\text{N}_2$  dissociation (Table 3, process 2), a key process in the LH mechanism for ammonia synthesis; for the Fe system the process has an activation barrier of  $0.708$  eV, and is exothermic by  $-0.436$ , whereas a lower barrier and even greater exothermicity was reported for the Co system ( $E_A = 0.24$  eV,  $\Delta E = -1.86$  eV). Whilst  $\text{N}_2$  dissociation appears to be both more kinetically and thermodynamically favourable over the Co system compared to the Fe system, one must bear in mind that the preceding  $\text{N}_2$  adsorption is more exothermic for the Fe system, hence it is likely that the overall pathway for  $\text{N}_2$  adsorption from the gas phase, and subsequently dissociation, is more facile for the Fe system, given that both processes are moderately exothermic and the dissociation process has only a moderate activation barrier.



## Comparison of hydrogenation processes and insights into activity of quaternary metal nitrides

Whilst an examination of the reaction profiles for the two mechanisms for both the Fe system investigated in the present work, and the Co system in previous computational studies, shows broadly similar behaviour, there are a few key differences that could help to identify limitations to the activity of both catalysts, and thus inform the future development of, for example, highly active ammonia synthesis catalysts based on the quaternary  $\text{Co}_{3-x}\text{Fe}_x\text{Mo}_3\text{N}$  system, with an optimal Co : Fe ratio.

As has already been discussed, the  $\text{N}_2$  activation behaviour of the Co and Fe systems is broadly similar, although in terms of hydrogenation, it appears that these processes are activated more for the Fe system. Indeed, examining the LH pathways for the two systems, it can be seen that activation barriers are consistently higher for the Fe system than the corresponding activation barriers for the Co system. The key structural difference appears to lie in the coordination environment of the  $\text{NH}^*$ ,  $\text{NH}_2^*$  and  $\text{NH}_3^*$  intermediates, with the calculations implying a greater stabilisation of these intermediates at the Fe–Mo interfacial sites compared to the corresponding Co–Mo sites in the Co system. Similarly, whilst the ER–MvK mechanism provides a less activated mechanistic pathway for both systems, it can be seen that whilst the initial hydrogenation processes are less activated for the Fe system, the latter hydrogenation processes are more so, once again reflecting the greater stability of these intermediates at the N vacancy site.

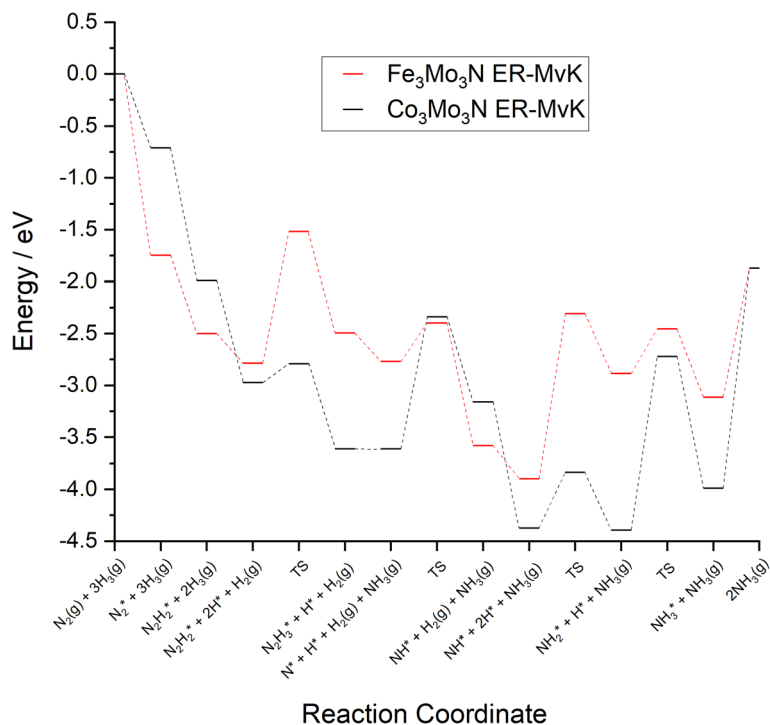


Fig. 18 Computed reaction profiles comparing the ER–MvK mechanism for ammonia synthesis on  $\text{Fe}_3\text{Mo}_3\text{N}$  (red) and for  $\text{Co}_3\text{Mo}_3\text{N}$  (black).<sup>35</sup>





To compare the more accessible ER–MvK mechanism for both the  $\text{Fe}_3\text{Mo}_3\text{N}$  and  $\text{Co}_3\text{Mo}_3\text{N}$  systems, a reaction profile illustrating this mechanism for the two systems is presented in Fig. 18, based on the results presented in this work and the previous literature on  $\text{Co}_3\text{Mo}_3\text{N}$ .<sup>35</sup> Whilst the reaction profiles are broadly similar, the general trend of the initial hydrogenation processes being less activated, and latter ones more activated, for the  $\text{Fe}_3\text{Mo}_3\text{N}$  system is clearly evident. In particular, it is notable that the highest activation barriers, which are likely to correspond to the overall rate-limited elementary processes, are comparable, even if they do not correspond to the same process. Namely, the activation barrier for the  $\text{NH}^*$  hydrogenation process is much higher for  $\text{Fe}_3\text{Mo}_3\text{N}$  than for  $\text{Co}_3\text{Mo}_3\text{N}$ , and is the most energy-demanding process for  $\text{Fe}_3\text{Mo}_3\text{N}$  (Table 1, process 8); yet as illustrated in Fig. 18, the most energy-demanding processes for  $\text{Co}_3\text{Mo}_3\text{N}$  correspond to  $\text{NH}_2^*$  hydrogenation, and evolution of the second equivalent of  $\text{NH}_3$  are comparable to that of the most energy-demanding process for  $\text{Fe}_3\text{Mo}_3\text{N}$ . This explains the high activity observed for  $\text{Fe}_3\text{Mo}_3\text{N}$  experimentally; indeed, it seems likely, based on the calculations performed in the present work, that the key difference between the two systems lies primarily in the greater resistance of  $\text{Fe}_3\text{Mo}_3\text{N}$  to loss of lattice N, which in turn reduces the concentration of active N vacancy sites compared to  $\text{Co}_3\text{Mo}_3\text{N}$ , resulting in overall lower ammonia production.

Based on these observations, we can suggest that a possible means by which the mixed quaternary Co/Fe system can enhance ammonia synthesis is by combining the greater ease of N vacancy formation (thereby increasing the concentration of active sites for the ER–MvK mechanism, which is the less activated for both the Fe and Co systems) associated with the Co system, along with the weaker binding of key intermediates at the Co–Mo interface and N vacancy site, with the greater extent of  $\text{N}_2$  activation and lower barriers for initial hydrogenation processes associated with the Fe system. We therefore speculate that optimal catalytic activity could be tuned by careful control of the Co : Fe ratio in the quaternary system, which combined with the promotion and doping strategies applied to the ternary systems, could enable highly active and stable ammonia synthesis catalysts that can operate under mild conditions.

## Conclusions

The calculations reported in the present work reveal that, like the isostructural  $\text{Co}_3\text{Mo}_3\text{N}$  system, the  $\text{Fe}_3\text{Mo}_3\text{N}$  system affords low activation barriers for ammonia synthesis *via* the ER–MvK mechanism, and in particular the Fe system has lower barriers for initial hydrogenation processes *via* the hydrazine-like intermediate. However, the vacancy formation energy for  $\text{Fe}_3\text{Mo}_3\text{N}$  is more endothermic than for  $\text{Co}_3\text{Mo}_3\text{N}$ , and as illustrated by the *ab initio* thermodynamics study, it is anticipated that  $\text{Fe}_3\text{Mo}_3\text{N}$  would feature lower concentrations of surface N vacancies compared to  $\text{Co}_3\text{Mo}_3\text{N}$ , in line with the experimentally well-observed tendency of the Fe system to be resistant to loss of lattice nitrogen. It is also notable that whilst the ER–MvK mechanism was determined to be the less activated pathway for both systems, the dissociative LH mechanism is more accessible on the Fe system since the initial adsorption of  $\text{N}_2$  is considerably more exothermic compared to the Co system, thus enabling the initial  $\text{N}_2$  activation process, although higher activation barriers were reported for latter



hydrogenation processes in the LH mechanism. Considering this, and the broadly similar features of the ammonia synthesis mechanisms for the two ternary metal nitride systems, it seems likely that the high activity of the  $\text{Fe}_3\text{Mo}_3\text{N}$  system reported experimentally can be attributed to the lower vacancy concentration, and thus lower concentration of active sites for the favoured ER–MvK mechanism, being partially compensated by the existing possibility for  $\text{N}_2$  hydrogenation to take place *via* the LH mechanism, reflecting the well-established high activity of promoted Fe catalysts used in industry.

The present work provides useful insights into the activity of metal nitride catalysts and it is intended that future work will explore not only promotion of the  $\text{Fe}_3\text{Mo}_3\text{N}$  system, but also the quaternary  $\text{Co}_{3-x}\text{Fe}_x\text{Mo}_3\text{N}$  system, which will be informed by the present work and the existing previous literature for the  $\text{Co}_3\text{Mo}_3\text{N}$  system.

## Conflicts of interest

The authors declare that there are no conflicts of interest.

## Acknowledgements

The authors thank the EPSRC/UKRI (EP/T028629/1) for financial support of this project, and the UK Catalysis Hub Consortium (funded by EPSRC (Grants EP/R026815/1)) for the provision of additional resources. The authors acknowledge the STFC (SCARF) and UK National Supercomputing Service (ARCHER2) for the provision of computational resources, the latter enabled *via* membership of the MCC (EP/L000202).

## References

- 1 *Scaling Ammonia Production For The World's Food Supply*, <https://www.forbes.com/sites/mitsubishiheavyindustries/2021/10/29/scaling-ammonia-production-for-the-worlds-food-supply/?sh=63a47ef968d1>, accessed 28 September 2022.
- 2 *World population projected to reach 9.8 billion in 2050, and 11.2 billion in 2100*, <https://www.un.org/development/desa/en/news/population/world-population-prospects-2017.html>, accessed 28 September 2022.
- 3 *Ammonia Market – Growth, Trends, COVID-19 Impact, and Forecasts (2022–2027)*, <https://www.mordorintelligence.com/industry-reports/ammonia-market>, accessed 28 September 2022.
- 4 J. Humphreys, R. Lan and S. Tao, *Advanced Energy and Sustainability Research*, 2021, **2**, 2000043.
- 5 J. W. Erisman, M. A. Sutton, J. Galloway, Z. Klimont and W. Winiwarter, *Nat. Geosci.*, 2008, **1**, 636–639.
- 6 *Ammonia: Zero-Carbon Fertiliser, Fuel and Energy Store*, <https://royalsociety.org/-/media/policy/projects/green-ammonia/green-ammonia-policy-briefing.pdf>, accessed 28 September 2022.
- 7 S. Ghavam, M. Vahdati, I. A. G. Wilson and P. Styring, *Front. Energy Res.*, 2021, **9**, 1–19.



- 8 *Electrochemical Ammonia Synthesis from Water and Nitrogen using Solid State Ion Conductors*, <https://www.ammoniaenergy.org/paper/electrochemical-ammonia-synthesis-from-water-and-nitrogen-using-solid-state-ion-conductors/>, accessed 28 September 2022.
- 9 L. Wang, M. Xia, H. Wang, K. Huang, C. Qian, C. T. Maravelias and G. A. Ozin, *Joule*, 2018, **2**, 1055–1074, <https://www.sciencedirect.com/science/article/pii/S2542435118301788>.
- 10 F. Haber, in *Nobel Lecture*, 1920, pp. 328–340.
- 11 G. Ertl, *Catal. Rev. Sci. Eng.*, 1980, **21**, 201–223.
- 12 M. Bowker, *Catal. Today*, 1992, **12**, 153–163.
- 13 Á. Logadóttir and J. K. Nørskov, *J. Catal.*, 2003, **220**, 273–279.
- 14 C. J. Zhang, M. Lynch and P. Hu, *Surf. Sci.*, 2002, **496**, 221–230.
- 15 C. D. Zeinalipour-Yazdi, J. S. J. Hargreaves and C. R. A. Catlow, *J. Phys. Chem. C*, 2015, **119**, 28368–28376.
- 16 J. S. J. Hargreaves, *Appl. Petrochem. Res.*, 2014, **4**, 3–10.
- 17 L. Volpe and M. Boudart, *J. Phys. Chem.*, 1986, **90**, 4874–4877.
- 18 W. Zheng, T. P. Cotter, P. Kaghazchi, T. Jacob, B. Frank, K. Schlichte, W. Zhang, D. S. Su, F. Schüth and R. Schlögl, *J. Am. Chem. Soc.*, 2013, **135**, 3458–3464.
- 19 N. Segal, *J. Catal.*, 1967, **8**, 105–112.
- 20 N. Segal and F. Sebba, *J. Catal.*, 1967, **8**, 113–119.
- 21 D. A. King, *J. Catal.*, 1965, **4**, 253–259.
- 22 D. A. King and F. Sebba, *J. Catal.*, 1965, **4**, 430–439.
- 23 R. Kojima and K. I. Aika, *Appl. Catal., A*, 2001, **209**, 317–325.
- 24 R. Kojima, H. Enomoto, M. Muhler and K. I. Aika, *Appl. Catal., A*, 2003, **246**, 311–322.
- 25 G. I. Panov and A. S. Kharitonov, *React. Kinet. Catal. Lett.*, 1985, **29**, 267–274.
- 26 R. Kojima and K. Aika, *Appl. Catal., A*, 2001, **215**, 149–160.
- 27 R. Kojima and K. Aika, *Appl. Catal., A*, 2001, **218**, 121–128.
- 28 R. Kojima and K.-I. Aika, *Appl. Catal., A*, 2001, **219**, 157–170.
- 29 C. J. H. Jacobsen, S. Dahl, B. G. S. Clausen, S. Bahn, A. Logadóttir and J. K. Nørskov, *J. Am. Chem. Soc.*, 2001, **123**, 8404–8405.
- 30 C. J. H. Jacobsen, *Chem. Commun.*, 2000, 1057–1058.
- 31 A. Boisen, S. Dahl and C. J. H. Jacobsen, *J. Catal.*, 2002, **208**, 180–186.
- 32 S. M. Hunter, D. H. Gregory, J. S. J. Hargreaves, M. Richard, D. Duprez and N. Bion, *ACS Catal.*, 2013, **3**, 1719–1725.
- 33 C. D. Zeinalipour-Yazdi, J. S. J. Hargreaves and C. R. A. Catlow, *J. Phys. Chem. C*, 2016, **120**, 21390–21398.
- 34 C. D. Zeinalipour-Yazdi, J. S. J. Hargreaves, S. Laassiri and C. R. A. Catlow, *Phys. Chem. Chem. Phys.*, 2018, **20**, 21803–21808.
- 35 C. D. Zeinalipour-Yazdi, J. S. J. Hargreaves and C. R. A. Catlow, *J. Phys. Chem. C*, 2018, **122**, 6078–6082.
- 36 C. D. Zeinalipour-Yazdi, J. S. J. Hargreaves, S. Laassiri and C. R. A. Catlow, *R. Soc. Open Sci.*, 2021, **8**, DOI: [10.1098/rsos.210952](https://doi.org/10.1098/rsos.210952).
- 37 D. Mckay, PhD thesis, University of Glasgow, 2008.
- 38 S. M. Hunter, PhD thesis, University of Glasgow, 2012.
- 39 A. Daisley, L. Costley-Wood and J. S. J. Hargreaves, *Top. Catal.*, 2021, **64**, 1021–1029.



- 40 G. Kresse and J. Hafner, *Phys. Rev. B: Condens. Matter Mater. Phys.*, 1993, **47**, 558–561.
- 41 G. Kresse and J. Hafner, *Phys. Rev. B: Condens. Matter Mater. Phys.*, 1994, **49**, 14251–14269.
- 42 G. Kresse and J. Furthmüller, *Comput. Mater. Sci.*, 1996, **6**, 15–50.
- 43 G. Kresse and J. Furthmüller, *Phys. Rev. B: Condens. Matter Mater. Phys.*, 1996, **54**, 11169–11186.
- 44 H. Monkhorst and J. Pack, *Phys. Rev. B: Solid State*, 1976, **13**, 5188–5192.
- 45 P. E. Blöchl, *Phys. Rev. B: Condens. Matter Mater. Phys.*, 1994, **50**, 17953–17979.
- 46 G. Kresse, *Phys. Rev. B: Condens. Matter Mater. Phys.*, 1999, **59**, 1758–1775.
- 47 S. Grimme, J. Antony, S. Ehrlich and H. Krieg, *J. Chem. Phys.*, 2010, **132**, 154104.
- 48 S. Grimme, S. Ehrlich and L. Goerigk, *J. Comput. Chem.*, 2011, **32**, 1456–1465.
- 49 NIST Webbook, <https://webbook.nist.gov/chemistry/>, accessed 28 September 2022.
- 50 K. Reuter, *Catal. Lett.*, 2016, **146**, 541–563.
- 51 K. Reuter and M. Scheffler, *Phys. Rev. B: Condens. Matter Mater. Phys.*, 2003, **67**, 205424.
- 52 J. Rogal and K. Reuter, *Ab Initio Atomistic Thermodynamics for Surfaces: A Primer, Experiment, Modeling and Simulation of Gas-Surface Interactions for Reactive Flows in Hypersonic Flights*, 2007, pp. 2-1–2-18.
- 53 M. Bollinger, K. Jacobsen and J. Nørskov, *Phys. Rev. B: Condens. Matter Mater. Phys.*, 2003, **67**, 85410–85427.
- 54 M. Moser, V. Paunović, Z. Guo, L. Szentmiklósi, M. G. Hevia, M. Higham, N. López, D. Teschner and J. Pérez-Ramírez, *Chem. Sci.*, 2016, **7**, 2996–3005.
- 55 A. Daisley and J. S. J. Hargreaves, *J. Energy Chem.*, 2019, **39**, 170–175.
- 56 T. Wang and F. Abild-Pedersen, *Proc. Natl. Acad. Sci. U. S. A.*, 2021, **118**, 1–5.
- 57 J. G. Chen, R. M. Crooks, L. C. Seefeldt, K. L. Bren, R. Morris Bullock, M. Y. Darensbourg, P. L. Holland, B. Hoffman, M. J. Janik, A. K. Jones, M. G. Kanatzidis, P. King, K. M. Lancaster, S. V. Lymer, P. Pfrohm, W. F. Schneider and R. R. Schrock, *Science*, 2018, **360**, 873–880.
- 58 K. P. Huber and G. Herzberg, *Molecular Spectra and Molecular Structure*, Springer US, Boston, MA, 1979.
- 59 D. McKay, J. S. J. Hargreaves, J. L. Rico, J. L. Rivera and X. L. Sun, *J. Solid State Chem.*, 2008, **181**, 325–333.

